

Article

# Effect of Al<sub>2</sub>O<sub>3</sub> on Microstructure and Corrosion Characteristics of Al/Al<sub>2</sub>O<sub>3</sub> Composite Coatings Prepared by Cold Spraying

Wei Jiang , Xin Shen, Zhiyuan Wang, Yang Liu, Xiaohua Zhang, Enhao Wang and Junxin Zhang

School of Materials Science and Chemical Engineering, Harbin University of Science and Technology, Harbin 150040, China; shenxinbwjl@163.com (X.S.); wangzhiyuan@hrbust.edu.cn (Z.W.); yang\_liu@hrbust.edu.cn (Y.L.); zxhhrbu@hrbust.edu.cn (X.Z.); enhaowang@hrbeu.edu.cn (E.W.); junxin\_zhang2020@163.com (J.Z.)

\* Correspondence: jiangwei@hrbust.edu.cn

**Abstract:** Cold spraying was used to prepare Al/Al<sub>2</sub>O<sub>3</sub> composite coatings. The Al<sub>2</sub>O<sub>3</sub> content was controlled to increase the mechanical property and corrosion resistance of the composite coating. The inclusion of Al<sub>2</sub>O<sub>3</sub> particles results in considerable plastic deformation of Al particles and grain size refinement in the coating. Additionally, the coating's surface roughness decreased from 24.63 μm to 9.02 μm, and the porosity decreased from 6.34% to 2.07%. The increase in microhardness of the composite coatings was attributed to the combined effect of residual compressive stress, second phase strengthening of Al<sub>2</sub>O<sub>3</sub>, and plastic hardening of Al particles. The electrochemical test results indicate that the mass fractions of Al<sub>2</sub>O<sub>3</sub> significantly affected the corrosion resistance of the Al/Al<sub>2</sub>O<sub>3</sub> composite coating. Compared to the Al coating, the composite coating exhibited improved corrosion resistance, with a reduction in corrosion current density from  $1.09 \times 10^{-3}$  A/cm<sup>2</sup> to  $2.67 \times 10^{-6}$  A/cm<sup>2</sup> and an increase in corrosion potential from  $-1.57$  V to  $-1.14$  V. However, when the alumina particle content exceeded 17.7%, it led to more Al<sub>2</sub>O<sub>3</sub> particle breakage, increasing the weak bonding interfaces in the composite coating, and consequently reducing its corrosion resistance.

**Keywords:** composite coating; cold spraying; microstructure; corrosion resistance



**Citation:** Jiang, W.; Shen, X.; Wang, Z.; Liu, Y.; Zhang, X.; Wang, E.; Zhang, J. Effect of Al<sub>2</sub>O<sub>3</sub> on Microstructure and Corrosion Characteristics of Al/Al<sub>2</sub>O<sub>3</sub> Composite Coatings Prepared by Cold Spraying. *Metals* **2024**, *14*, 179. <https://doi.org/10.3390/met14020179>

Academic Editor: Hannu Hänninen

Received: 7 January 2024

Revised: 22 January 2024

Accepted: 28 January 2024

Published: 1 February 2024



**Copyright:** © 2024 by the authors. Licensee MDPI, Basel, Switzerland. This article is an open access article distributed under the terms and conditions of the Creative Commons Attribution (CC BY) license (<https://creativecommons.org/licenses/by/4.0/>).

## 1. Introduction

Among the coating materials, aluminum coating is extensively utilized in aviation and space, transportation, marine engineering equipment, and electronics owing to its excellent anti-corrosion properties, and its electrical and thermal conductivity [1,2]. However, the application of aluminum coatings was limited due to its relatively low hardness and insufficient wear resistance. Therefore, the current research focus is on how to modify the Al coating to improve its overall performance. Aluminum metal matrix composite (Al-MMC) coatings containing ceramic reinforcements are a type of high-performance surface-modified coating [3,4]. Ceramic particles in Al-MMC materials can influence the degree of deformation of Al particles [5], resulting in a decrease in porosity [6] and roughness, and an increase in hardness [7], abrasion resistance [8], and corrosion resistance [9] of the coating, and it can also change the physical properties of the coating such as the strength-to-density ratio and high-temperature performance [10].

Cold spraying is a common method for preparing composite coatings [11]. Cold spraying technology is a surface coating technology developed based on the principles of gas dynamics and high-speed collision dynamics [12–14]. Cold spraying technology has the characteristics of high spraying rate, the high strength of the sprayed bonding layer, dense coating, and low temperature compared to preparation methods such as thermal spraying [15], electroplating [16], laser cladding [17], and chemical vapor deposition (CVD) [18]. In recent years, scholars have investigated the properties of cold-sprayed Al-MMC coatings. For instance, in their study, Wang et al. [19] investigated the corrosion characteristics of Al-MMC coatings and determined their anticorrosion mechanism. They

found that the ceramic particle content and porosity of composite coatings have a great influence on corrosion resistance. However, the deposition efficiency and coating porosity of ceramic particles are related to the sizes of ceramic particles. Yang et al. [20] prepared an Al/Al<sub>2</sub>O<sub>3</sub> composite coating by spraying the raw material containing Al<sub>2</sub>O<sub>3</sub> particles onto the surface of the substrate using the cold spraying technique. The results show that the composite coating had the best corrosion resistance when the Al<sub>2</sub>O<sub>3</sub> content was 20 vol. %. Xie et al. [21] prepared TiB<sub>2</sub> particle reinforced 7075Al composite coatings using the cold spraying technique, and reduced coating porosity while simultaneously improving the corrosion resistance of the coating. Qiu et al. [22] mixed spherical, irregular, and spherical-irregular Al<sub>2</sub>O<sub>3</sub> particles into cold spray powder materials and studied the influence of Al<sub>2</sub>O<sub>3</sub> morphology on coating performance. The research indicates that spherical particles have the best mechanical interlocking connection with the substrate and the lowest surface porosity. Wang et al. [23] utilized the cold spraying technique to prepare Al/Al<sub>2</sub>O<sub>3</sub> composite coatings and investigated the microstructure and nanomechanical properties of the composite coatings in orthogonal and normal planes. The experimental results show that the degree of plastic deformation of the Al particles increases due to the tamping effect of the high-speed Al<sub>2</sub>O<sub>3</sub> particles, leading to grain refinement along the grain boundaries of the composite coating, resulting in increased hardness and reduced friction coefficient. Many researchers have investigated the mechanical characteristics and corrosion resistance of cold-sprayed Al-MMC coatings [24,25], but comparatively little work has been done on the effect of the microstructure of Al-MMC coatings on the corrosion mechanism and process.

This paper aims to further explore and elucidate the effect of doping Al<sub>2</sub>O<sub>3</sub> particles on the microstructure evolution and performance improvement of Al/Al<sub>2</sub>O<sub>3</sub> composite coatings, building upon previous studies. The fabrication of Al/Al<sub>2</sub>O<sub>3</sub> composite coatings on the surface of No. 45 steel was carried out using the cold spraying technique, with varying Al<sub>2</sub>O<sub>3</sub> contents (mass fractions of 0%, 17.7%, 25.5%, 33.3%). A characterization of the microhardness and electrochemical corrosion behavior of the Al/Al<sub>2</sub>O<sub>3</sub> composite coatings was conducted, along with an analysis of microstructure evolution.

## 2. Materials and Methods

### 2.1. Experimental Materials

Commercial spherical Al powder (diameter 20 μm) and Al<sub>2</sub>O<sub>3</sub> powder (diameter 20 μm) were used in the cold spray experiment, as illustrated in Figure 1a,b. The substrate material selected was No. 45 steel, the composition of which is detailed in Table 1. The dimensions of the substrate were 30 mm × 30 mm × 5 mm.

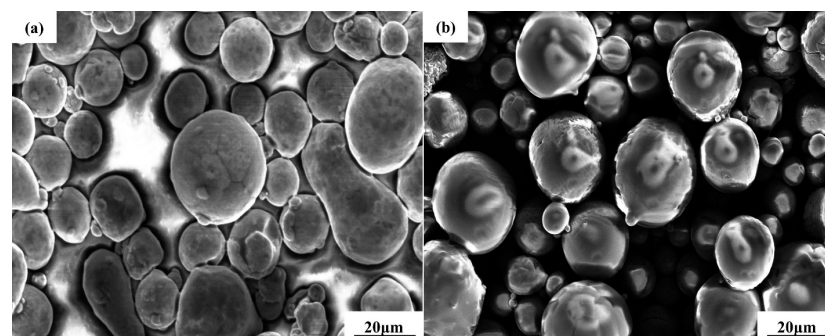


**Figure 1.** Morphologies of Al powder (a) and Al<sub>2</sub>O<sub>3</sub> particles (b).

**Table 1.** Chemical composition of No. 45 steel.

C	Mn	Si	Cr	Ni	Cu
0.42–0.50%	0.50–0.80%	0.17–0.37%	≤0.25%	≤0.30%	≤0.25%

The carrier gas for cold spraying was compressed air at a pressure of 1.0 MPa and a temperature of 500 °C. The spray gun outlet was positioned 10 mm away from the substrate, while the traveling speed was set at 60 mm/s. The coating thickness obtained by cold spraying was about 400–500 µm.

## 2.2. Test Methods

The surface cross-section morphology of the cold-sprayed coatings was observed using a scanning electron microscope (SEM, Hitachi, Tokyo, Japan, SU5000). The chemical composition of the coatings was analyzed using an energy dispersive spectrometer (EDS, Ultimately Max40, Oxford Instruments, Abingdon, UK), and the microstructural evolution of the coatings was characterized using electron backscatter diffraction (EBSD, Symmetry, Oxford Instruments, Abingdon, UK). Porosity statistics of the coatings were obtained from SEM images of five different areas of the coating cross-section using Image J software (v1.52a, NIH, Rockville, MD, USA). The phase composition of the coatings was analyzed using an X-ray diffractometer (XRD, X'Pert PRO, Panalytical, Almelo, The Netherlands). Microhardness measurements of the samples were conducted using a Vickers hardness tester (HVS-1000Z, Shangcai, Shanghai, China) with a load of 50 g and a holding time of 15 s. Measurements were taken three times at 20 µm intervals along the depth direction. The surface roughness of the coating was measured using an ultra-depth-of-field three-dimensional microscope (OLYMPUS, Tokyo, Japan, DSX1000).

The electrochemical properties of the Al/Al<sub>2</sub>O<sub>3</sub> composite coating were determined using an electrochemical workstation (VMP3, BioLogic, Seyssinet-Pariset, France) at 25 ± 1 °C in a 3.5 wt. % NaCl solution. In a three-electrode system, the working electrode (WE) was the coating, the reference electrode (SCE) was an Ag/AgCl electrode, and the counter electrode (CPE) was a platinum electrode. The reference electrode was positioned within 3 mm of the sample surface, and the counter electrode was placed at an equal distance from the other two electrodes. The open circuit potential (OCP) of the sample was measured. The electrochemical impedance spectroscopy (EIS) of the composite coating was evaluated at frequencies ranging from 10 mHz to 100 kHz, with the voltage amplitude was OCP ± 10 mV. Subsequently, potentiodynamic polarization curves of the samples were obtained. The electrochemical data of the cold-sprayed coatings were determined by fitting the potentiodynamic polarization curves by Tafel extrapolation. The tested area of the samples was 1 cm<sup>2</sup>. All electrochemical tests were repeated at least three times for better accuracy.

## 3. Results

### 3.1. XRD Analysis

The XRD test results of the coating are shown in Figure 2. The results show that in the Al coating, the diffraction peaks were located at 38.5°, 44.7°, 65.1°, and 78.2°, which correspond to the (111), (200), (220), and (311) crystal planes, respectively. In addition, in the Al/Al<sub>2</sub>O<sub>3</sub> composite coatings with three different Al<sub>2</sub>O<sub>3</sub> contents, typical characteristic peaks of Al<sub>2</sub>O<sub>3</sub> appeared at 52.6°, 57.5°, and 68.2°. These correspond to crystal planes (024), (116) and (300), respectively. As can be seen from the Figure 2, no new phases appeared during the composite coating-manufacturing process. The right side of Figure 2 shows a magnified partial XRD spectrum from 37° to 40°, indicating a shift of characteristic peaks toward higher angles. This phenomenon was due to stress changes within the coating. The compressive residual stress was caused by the shot peening effect of Al<sub>2</sub>O<sub>3</sub> particles on Al coating. The presence of compressive residual stresses induced a reduction in the interplanar crystal spacing, accompanied by a shift in the characteristic peaks of Al phase to higher angles. Residual compressive stress is beneficial to the improvement of the mechanical and electrochemical properties of the composite coating by reducing the porosity of the coating and preventing microcrack propagation.

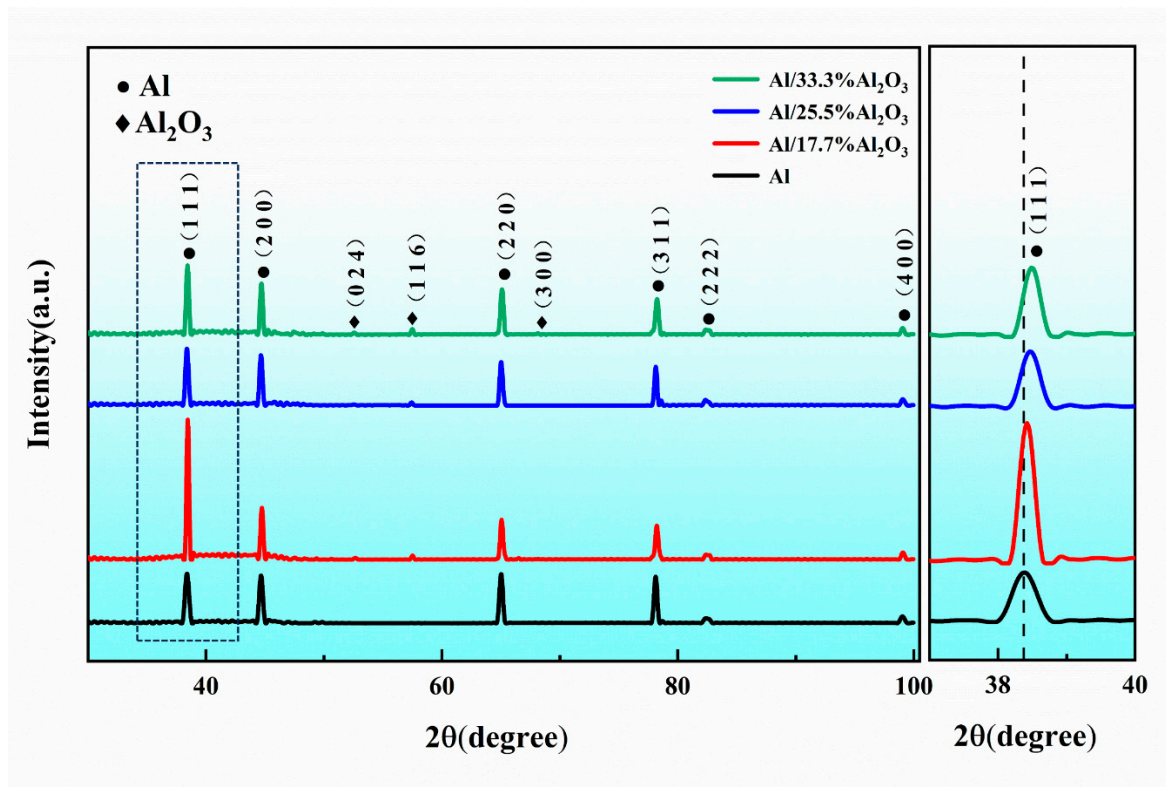


Figure 2. XRD patterns of the cold spraying coatings.

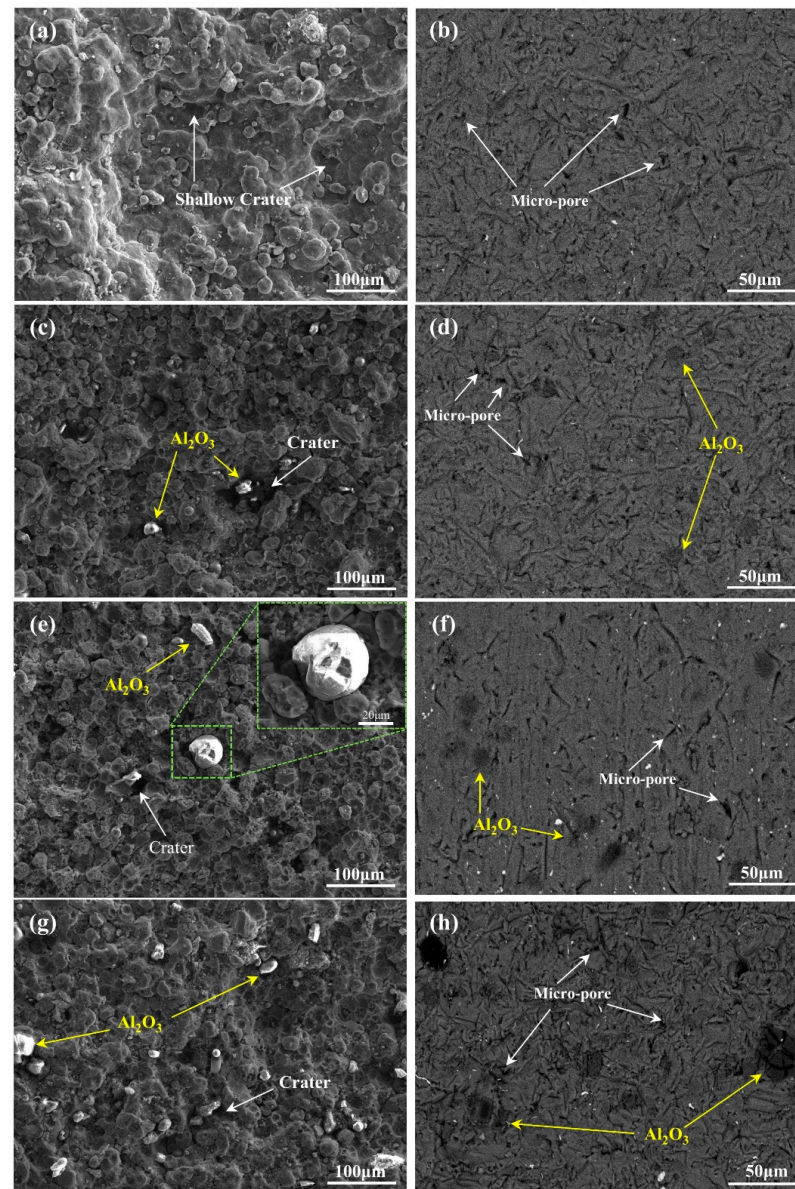
### 3.2. Surface Morphology of the Coating

Figure 3 presents the micro-morphology of the Al coating and the Al/Al<sub>2</sub>O<sub>3</sub> composite coatings. In Figure 3a, the surface morphology of the Al coating reveals shallow craters and spherical Al particles. This occurrence is attributed to the relatively small plastic deformation experienced by the aluminum particles, allowing some particles to maintain their spherical shape. In contrast, the Al/Al<sub>2</sub>O<sub>3</sub> composite coating does not exhibit a similar phenomenon. The peening action of the Al<sub>2</sub>O<sub>3</sub> particles leads to the significant secondary plastic deformation of the co-deposited Al particles, resulting in the flattening of the spherical Al particles. Figure 3c illustrates that the coating surface displays deeper craters due to the presence of embedded spherical Al<sub>2</sub>O<sub>3</sub> particles. Furthermore, Figure 3e demonstrates that an increase in the percentage of Al<sub>2</sub>O<sub>3</sub> particles leads to the fragmentation of the embedded particles. Lastly, Figure 3g depicts the collision-induced breakage of some Al<sub>2</sub>O<sub>3</sub> particles, causing the detachment of certain embedded Al<sub>2</sub>O<sub>3</sub> particles from the coating.

As can be seen from Figure 3b,d,f,h, a small number of micropores developed between the particles. The process characteristics of cold spraying resulted in the formation of micropores in the deposited coating. In Figure 3h, it can be observed that with the increase in Al<sub>2</sub>O<sub>3</sub> content in the raw material, the Al<sub>2</sub>O<sub>3</sub> particles in the composite coating tended to change from internal cracks to fracture separation, which is consistent with the results observed in the surface microstructure. This indicates that the Al<sub>2</sub>O<sub>3</sub> particles deposited in the coating are more susceptible to being broken by the impact of the subsequent Al<sub>2</sub>O<sub>3</sub> particles with the increase in the Al<sub>2</sub>O<sub>3</sub> content in the raw material in the spraying process.

The porosity of the coatings was calculated from the cross-sectional images using Image J software, and the porosity data are shown in Table 2. The Al coating showed the highest porosity at around 6.34%. The composite coating's porosity decreased to 2.07% with an increase in Al<sub>2</sub>O<sub>3</sub> content to 17.7%. This decrease can be attributed to the compaction effect of the alumina particles. The hardness and density of Al<sub>2</sub>O<sub>3</sub> particles are higher than those of Al particles. Including Al<sub>2</sub>O<sub>3</sub> particles in the spraying process enhances the

deformation of the Al particles, resulting in the sealing of micropores and cracks in the coatings. However, the porosity of the composite coatings increased slightly with increasing  $\text{Al}_2\text{O}_3$  content. The porosity values of the Al/25.5%  $\text{Al}_2\text{O}_3$  and Al/33.3%  $\text{Al}_2\text{O}_3$  composite coatings were 3.39% and 3.59%, respectively. With increasing  $\text{Al}_2\text{O}_3$  concentration in the composite coating, the probability of collision between the  $\text{Al}_2\text{O}_3$  particles increases, resulting in more alumina particles being broken. Fractured  $\text{Al}_2\text{O}_3$  particles increase microporosity and microcracking in Al/ $\text{Al}_2\text{O}_3$  composite coatings, causing coating porosity to increase.



**Figure 3.** Surface and cross-section microstructures of Al coatings (a,b), Al/17.7%  $\text{Al}_2\text{O}_3$  composite coatings (c,d), Al/25.5%  $\text{Al}_2\text{O}_3$  composite coatings (e,f) and Al/33.3%  $\text{Al}_2\text{O}_3$  composite coatings (g,h).

**Table 2.** Porosity of the cold spraying coatings.

Specimen	Al	Al/17.7% $\text{Al}_2\text{O}_3$	Al/25.5% $\text{Al}_2\text{O}_3$	Al/33.3% $\text{Al}_2\text{O}_3$
Porosity (%)	$6.34 \pm 0.08$	$2.07 \pm 0.12$	$3.39 \pm 0.07$	$3.59 \pm 0.10$

### 3.3. Coating Hardness and Roughness

The microhardness distribution of coatings with different Al<sub>2</sub>O<sub>3</sub> contents is shown in Figure 4. With the increase in depth, the microhardness of the coating did not show a significant difference. This phenomenon is an indication that the Al<sub>2</sub>O<sub>3</sub> particles are uniform throughout the coating. The average hardness of the Al coating is 21.62 HV, and the average hardness of the Al/17.7% Al<sub>2</sub>O<sub>3</sub>, Al/25.5% Al<sub>2</sub>O<sub>3</sub>, and Al/33.3% Al<sub>2</sub>O<sub>3</sub> composite coatings are 47.25 HV, 48.54 HV, and 49.55 HV, respectively. The average hardness of the sprayed coating significantly increased when ceramic particles of Al<sub>2</sub>O<sub>3</sub> were added. This phenomenon can be attributed to three reasons. Firstly, the Al<sub>2</sub>O<sub>3</sub> particles enhanced the second phase-strengthening effect of the aluminum-based composite coating, thereby increasing its hardness. Secondly, the presence of ceramic particles created residual stress in the coatings, leading to changes in the crystal microstructure and grain morphology, consequently enhancing their hardness. Lastly, the addition of Al<sub>2</sub>O<sub>3</sub> particles refined the Al grain and increased the number of grain boundaries. The presence of grain boundaries inhibited dislocation movement, increasing the yield stress in the composite and consequently the average coating hardness. The increase in coating hardness was relatively low after the Al<sub>2</sub>O<sub>3</sub> content exceeded 17.7%. This was because, when a certain amount of reinforcement by ceramic particles occurred, the dislocation density significantly increased, leading to dislocation entanglement during dislocation movement. As a result, further dislocation movement is hindered, resulting in a relatively low increase in coating hardness.

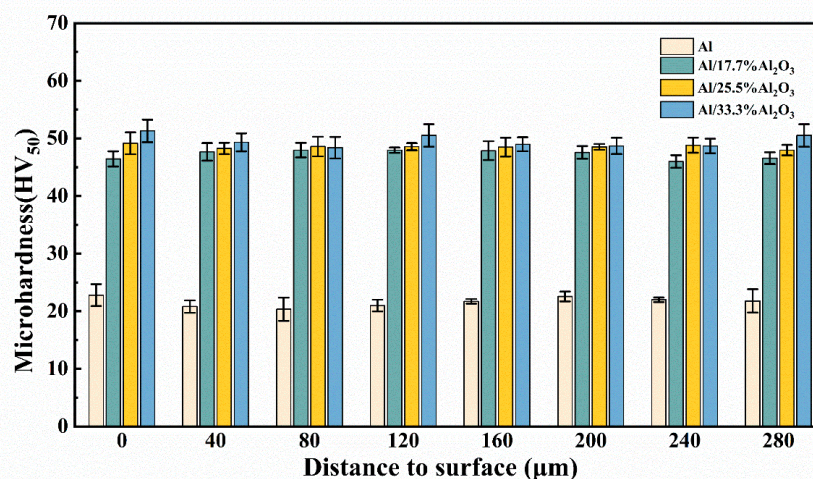


**Figure 4.** Microhardness profiles of cold spraying coatings along the coating cross-section.

Figure 5 shows the 3D surface morphology and surface root-mean-square roughness (Sq) of the Al coating, as well as the Al/17.7% Al<sub>2</sub>O<sub>3</sub>, Al/25.5% Al<sub>2</sub>O<sub>3</sub> and Al/33.3% Al<sub>2</sub>O<sub>3</sub> composite coatings, respectively. As the Al<sub>2</sub>O<sub>3</sub> concentration increased, the surface roughness of the composite coatings tended to decrease and then increase. The Al coating showed a surface roughness of 24.63 μm. The Al/17.7% Al<sub>2</sub>O<sub>3</sub> composite coating was 9.02 μm, the Al/25.5% Al<sub>2</sub>O<sub>3</sub> composite coating was 15.63 μm, and the Al/33.3% Al<sub>2</sub>O<sub>3</sub> composite coating was 16.94 μm. The incorporation of Al<sub>2</sub>O<sub>3</sub> particles resulted in a smoother composite coating surface. The 3D morphology of the coatings shows that the surface of the Al coating was very rough and wavy and the Al/Al<sub>2</sub>O<sub>3</sub> composite coating's surface was relatively flat. The addition of Al<sub>2</sub>O<sub>3</sub> particles caused the deformation of already coated Al particulates, gradually flattening the Al particles, and reducing the roughness of the coating. However, as the addition of Al<sub>2</sub>O<sub>3</sub> particles increased, the cooperative deformation ability of Al particles decreased, and the probability of a mutual impact of Al<sub>2</sub>O<sub>3</sub> particles rose, causing the Al<sub>2</sub>O<sub>3</sub> particles to fracture. The broken Al<sub>2</sub>O<sub>3</sub> particles were embedded in the coating surface, leading to a slight increase in the surface roughness of the coating.

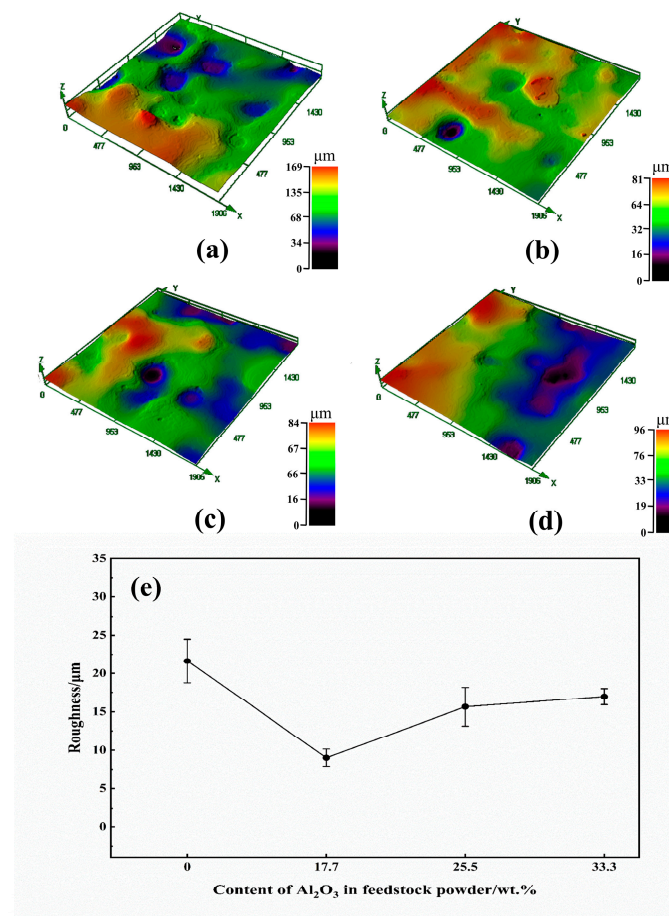


**Figure 5.** The 3D morphology of Al coatings (a), Al/17.7% Al<sub>2</sub>O<sub>3</sub> composite coatings (b), Al/25.5% Al<sub>2</sub>O<sub>3</sub> composite coatings (c) and Al/33.3% Al<sub>2</sub>O<sub>3</sub> composite coatings (d), and the roughness of the cold spray coating (e).

### 3.4. Corrosion Experiment

#### 3.4.1. Coating Electrochemical Corrosion Behavior

The potentiodynamic polarization curves of the cold spray coating measured in a 3.5 wt. % NaCl solution are shown in Figure 6a. The open circuit potentials (OCP) of the pure Al coating, and the Al/17.7% Al<sub>2</sub>O<sub>3</sub>, Al/25.5% Al<sub>2</sub>O<sub>3</sub>, and Al/33.3% Al<sub>2</sub>O<sub>3</sub> composite coatings, were  $-1.46$  V,  $-1.08$  V,  $-1.25$  V, and  $-1.20$  V, respectively. The OCP values of the Al coatings were more negative compared to the Al/Al<sub>2</sub>O<sub>3</sub> composite coatings, which can be a preliminary indication that the incorporation of Al<sub>2</sub>O<sub>3</sub> particles improved the corrosion resistance of the coating. The corrosion potential ( $E_{\text{CORR}}$ ) and corrosion current density ( $I_{\text{CORR}}$ ) for different samples are presented in Table 3. The  $E_{\text{CORR}}$  and  $I_{\text{CORR}}$  of the Al coating were  $-1.58$  V and  $1.09 \times 10^{-3}$  A/cm<sup>2</sup>. For the Al/17.7% Al<sub>2</sub>O<sub>3</sub>, Al/25.5% Al<sub>2</sub>O<sub>3</sub>, and Al/33.3% Al<sub>2</sub>O<sub>3</sub> composite coatings, the  $E_{\text{CORR}}$  and  $I_{\text{CORR}}$  were  $-1.14$  V and  $2.67 \times 10^{-6}$  A/cm<sup>2</sup>,  $-1.25$  V and  $2.12 \times 10^{-5}$  A/cm<sup>2</sup>, and  $-1.22$  V and  $1.54 \times 10^{-5}$  A/cm<sup>2</sup>, respectively. Notably, the  $E_{\text{CORR}}$  of the Al/Al<sub>2</sub>O<sub>3</sub> composite coating exhibited an increase compared to that of the Al coating, concomitant with a decrease in  $I_{\text{CORR}}$ . The  $E_{\text{CORR}}$  serves as an indicator of corrosion difficulty, while  $I_{\text{CORR}}$  mirrors the rate of corrosion. The increase in  $E_{\text{CORR}}$  and the decrease in  $I_{\text{CORR}}$  indicate an improvement in the corrosion resistance of the composite coating. The  $E_{\text{CORR}}$  values of the Al/25.5% Al<sub>2</sub>O<sub>3</sub> and Al/33.3% Al<sub>2</sub>O<sub>3</sub> composite coatings were higher than that of the Al coating but lower than that of the Al/17.7% Al<sub>2</sub>O<sub>3</sub> composite coating. The  $I_{\text{CORR}}$  was lower than that of the Al coating but higher than that of the Al/17.7% Al<sub>2</sub>O<sub>3</sub> composite coating. The corrosion behavior of the coating is influenced by the content of Al<sub>2</sub>O<sub>3</sub> particles. The addition of Al<sub>2</sub>O<sub>3</sub> particles can make the coating denser and improve the corrosion resistance. However, the particle boundary between

Al particles and Al<sub>2</sub>O<sub>3</sub> particles provides a channel for the entry of NaCl solution. Al<sub>2</sub>O<sub>3</sub> particles undergo fragmentation due to excessive addition form more particle boundaries. Therefore, the corrosion resistance of the coating increases and then decreases with the increase in alumina content.

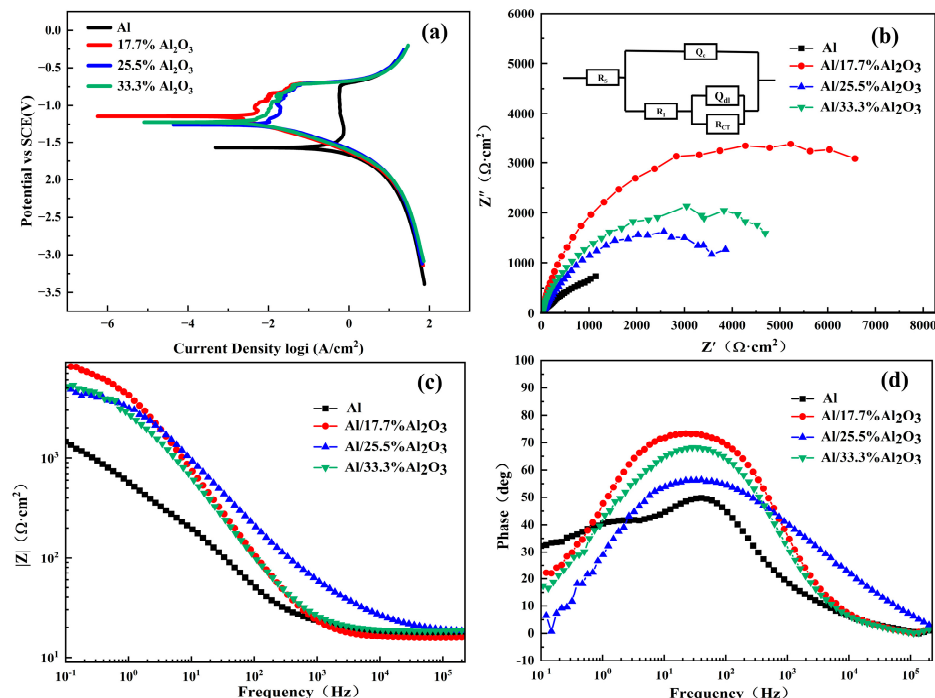


**Figure 6.** Potentiodynamic polarization curves (a), Nyquist plots (b), Bode modulus (c) and phase angle (d) spectra for cold-sprayed Al coatings and Al/Al<sub>2</sub>O<sub>3</sub> composite coatings.

**Table 3.** Results of Tafel extrapolation of potentiodynamic polarization curves and electrochemical data obtained via equivalent circuit fitting for cold-sprayed coatings.

Specimen	$E_{\text{corr}}$ (V)	$I_{\text{corr}}$ (A/cm <sup>2</sup> )	R <sub>p</sub> (Ω·cm <sup>2</sup> )	R <sub>s</sub> (kΩ·cm <sup>2</sup> )	R <sub>i</sub> (kΩ·cm <sup>2</sup> )	Q <sub>c</sub> (μF·cm <sup>-2</sup> )	n <sub>c</sub>	R <sub>ct</sub> (kΩ·cm <sup>2</sup> )	Q <sub>dl</sub> (μF·cm <sup>-2</sup> )	n <sub>dl</sub>
Al	-1.57	$1.09 \times 10^{-3}$	139.4	$1.72 \times 10^{-2}$	0.071	229.7	0.71	2.20	596.9	0.62
Al/17.7%Al <sub>2</sub> O <sub>3</sub>	-1.14	$2.67 \times 10^{-6}$	21,447.7	$1.58 \times 10^{-2}$	7.82	35.1	0.87	3.41	487.4	0.92
Al/25.5%Al <sub>2</sub> O <sub>3</sub>	-1.26	$2.12 \times 10^{-5}$	2579.6	$1.82 \times 10^{-2}$	2.04	50.4	0.70	2.91	25.9	0.98
Al/33.3%Al <sub>2</sub> O <sub>3</sub>	-1.22	$1.54 \times 10^{-5}$	6967.8	$1.84 \times 10^{-2}$	3.49	45.6	0.83	3.01	164.2	0.61

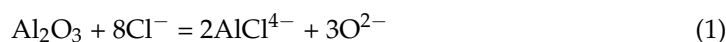
The corrosion resistance of Al/Al<sub>2</sub>O<sub>3</sub> composite coatings was evaluated using electrochemical impedance spectroscopy (EIS). Figure 6b depicts the Nyquist plots generated from tests conducted on cold-sprayed composite coatings immersed in a 3.5% NaCl solution. The diameter of the capacitive arc in the high-frequency region of the Nyquist diagram has a significant correlation with the corrosion resistance of the coatings. By adding ceramic particles, the arc diameter of the Al/Al<sub>2</sub>O<sub>3</sub> composite coating is made considerably larger than that of the pure aluminum coating at a high frequency. This disparity signifies a noteworthy enhancement in corrosion resistance for the composite coating featuring added alumina, as opposed to its pure aluminum counterpart. Among the Al/Al<sub>2</sub>O<sub>3</sub> composite coatings, the Al/17.7% Al<sub>2</sub>O<sub>3</sub> coating has the largest capacitive arc diameter. The capacitive arc diameter of the Al/33.3% Al<sub>2</sub>O<sub>3</sub> coating is slightly larger than the Al/25.5% Al<sub>2</sub>O<sub>3</sub> coating. Figure 6c,d shows the Bode plot obtained after impedance testing. According to previous studies [26], the magnitude of low-frequency impedance  $|Z|$  is positively correlated with corrosion resistance. From Figure 6c, we see that the  $|Z|$  of the Al/17.7% Al<sub>2</sub>O<sub>3</sub> composite coating was the largest, which also proves its best corrosion resistance. Figure 6d illustrates a phase diagram used for calculating the interfacial processes involved in impedance data. As shown in the figure, the phase diagrams of almost all coatings have

two peaks throughout the test, i.e., two time constants (TC). One is in the mid-frequency region (MF), indicating the presence of an oxide film on the coating surface. The other is in the low-frequency region (LF). The low-frequency region is characterized by pitting formation, which is due to the relaxation process of adsorbed substances (e.g.,  $\text{Cl}^-$ ) acquired in the vulnerable region [27], and the diffusion resistance in the system decreases with increasing  $\text{Al}_2\text{O}_3$  content, which corresponds to the porosity of the composite coating in Table 2.

The obtained electrochemical impedance spectroscopy can be fitted using the ZSimpWin software (v3.60, AMETEK Scientific Instruments, Berwyn, IL, USA), which helps in reflecting the electrochemical processes at the interface between the sample and the electrolyte. Figure 6b shows the fitted equivalent circuit, which indicates that the oxide film on the coating surface is not uniform [28]. In the figure,  $R_s$  is the solution resistance,  $R_{ct}$  is the charge transfer resistance of the aluminum coating, and  $R_l$  is the added resistance of the electrolyte within the localized corrosion site. Considering the non-ideal nature of the system, we used a constant phase element CPE (abbreviated as Q) instead of a pure capacitor [29,30].  $Q_c$  is an oxide film capacitor and  $Q_{dl}$  is a double-layer capacitor. The  $R_l$  and  $R_{ct}$  values derived from the fitting results are shown in Table 3. At low frequencies, the current cannot flow through the oxide film, only through the corrosion site. At high frequencies, the current can pass through the oxide film. The combined values of  $R_l$  and  $R_{ct}$  in the fitting results determine the corrosion resistance of the coating. A larger value of  $R_l + R_{ct}$  indicates the better corrosion resistance of the coating. The  $R_l + R_{ct}$  values of the coatings were  $2.27 \text{ k}\Omega\cdot\text{cm}^2$ ,  $11.23 \text{ k}\Omega\cdot\text{cm}^2$ ,  $4.95 \text{ k}\Omega\cdot\text{cm}^2$  and  $6.50 \text{ k}\Omega\cdot\text{cm}^2$ , respectively. The coatings' corrosion resistance were ranked, in descending, order as follows:  $\text{Al}/17.7\% \text{ Al}_2\text{O}_3 > \text{Al}/33.3\% \text{ Al}_2\text{O}_3 > \text{Al}/25.5\% \text{ Al}_2\text{O}_3 > \text{Al}$ . These results align with the potentiodynamic polarization curves. The mechanism of the improvement in the corrosion resistance of composite coatings is explained in detail in the discussion section.

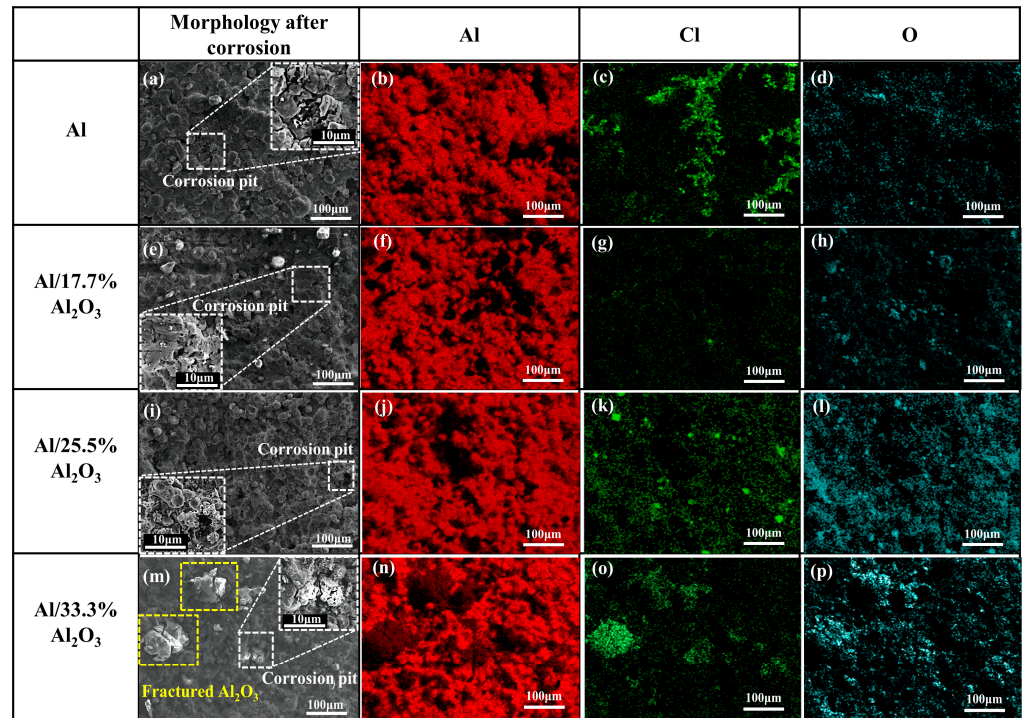
### 3.4.2. Surface Morphology after Electrochemical Corrosion

Figure 7 depicts the surface morphology and chemical element composition of the Al coating and  $\text{Al}/\text{Al}_2\text{O}_3$  composite coating after undergoing a corrosion test. The specific content of each element is presented in Table 4. Upon examination of Figure 7a,e,i,m, it was observed that the Al coating displayed significant corrosion holes, whereas the  $\text{Al}/\text{Al}_2\text{O}_3$  composite coating exhibited smaller corrosion holes, which is mainly attributed to pitting corrosion. Additionally, the pure Al coating demonstrated the highest Cl content at 2.66 wt. %. On the other hand, the composite coatings, namely,  $\text{Al}/17.7\% \text{ Al}_2\text{O}_3$ ,  $\text{Al}/25.5\% \text{ Al}_2\text{O}_3$ , and  $\text{Al}/33.3\% \text{ Al}_2\text{O}_3$ , showcased lower Cl contents at 0.40 wt. %, 1.18 wt. %, and 1.86 wt. %, respectively. The combination of morphology and data leads to the conclusion that the Al coating is more susceptible to corrosion. The  $\text{Cl}^-$  in the electrolyte reacted with the passivation film on the surface of the coating in a nucleophilic substitution reaction, resulting in the destruction of the passivation film. The reaction is as follows:



**Table 4.** EDS analysis results of the coating surface after corrosion.

Specimen	Al (wt. %)	Cl (wt. %)	O (wt. %)
Al	79.22	2.66	18.12
$\text{Al}/17.7\% \text{ Al}_2\text{O}_3$	80.26	0.40	19.33
$\text{Al}/25.5\% \text{ Al}_2\text{O}_3$	73.01	1.18	25.82
$\text{Al}/33.3\% \text{ Al}_2\text{O}_3$	69.08	1.86	37.16



**Figure 7.** Surface morphology and elemental maps after electrochemical corrosion of (a–d) Al coating, (e–h) Al/17.7% Al<sub>2</sub>O<sub>3</sub> composite coating, (i–l) Al/25.5% Al<sub>2</sub>O<sub>3</sub> composite coating, and (m–p) Al/33.3% Al<sub>2</sub>O<sub>3</sub> composite coating.

The whole reaction is equivalent to Cl<sup>−</sup> catalyzing the following reactions:

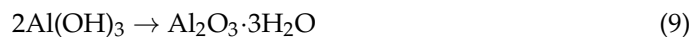
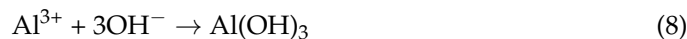


At the same time, the surface of the coating constituted a galvanic cell as the NaCl solution acts as an electrolyte. The cathode generated OH<sup>−</sup>, which led to a decrease in the PH value of the electrolyte, and the anode generated Al<sup>3+</sup>. The anode and cathode reacted as:



The corrosion resistance of the coating is negatively correlated with the content of Cl element. Cl<sup>−</sup> tended to accumulate in corrosive areas. From Figure 7m,o, we see that the Cl element was mainly concentrated at the bonding interface between the Al matrix and Al<sub>2</sub>O<sub>3</sub> particles. The bonding between Al particles and Al<sub>2</sub>O<sub>3</sub> particles was weak, and a weak bonding surface was present. The weak binding surface provided a channel for the electrolyte to enter the coating. When the amount of alumina particles added exceeded 17.7%, more alumina broke due to collisions. The broken alumina particles created additional weak bonding surfaces in the coating, resulting in reduced corrosion resistance. The O contents of the Al coating and the Al/17.7% Al<sub>2</sub>O<sub>3</sub>, Al/25.5% Al<sub>2</sub>O<sub>3</sub>, and Al/33.3% Al<sub>2</sub>O<sub>3</sub> composite coatings were 18.12 wt. %, 19.33 wt. %, 25.82 wt. %, and 37.16 wt. %, respectively. The surface oxygen contents of the coatings increased with the increase in Al<sub>2</sub>O<sub>3</sub> content. The main sources of O on the surface of the coating were (1) Al<sub>2</sub>O<sub>3</sub> particles containing the element O; also, (2) Al reacts with O<sub>2</sub> in the electrolyte to form Al<sub>2</sub>O<sub>3</sub>; (3) OH<sup>−</sup> generated by the cathodic reaction reacts with Al<sup>3+</sup> to form Al(OH)<sub>3</sub>, and (4) Al(OH)<sub>3</sub> is further converted to insoluble Al<sub>2</sub>O<sub>3</sub>·3H<sub>2</sub>O [31]. The reactions are as follows:





These reaction products covered the surface of the coating, making it more difficult for the coating to corrode further.

#### 4. Discussion

To further investigate the microstructural evolution of coatings with different alumina contents, EBSD analysis was performed on Al coatings and Al/17.7% Al<sub>2</sub>O<sub>3</sub> composite coatings. Figure 8a,d shows the IPF maps of the Al coating and Al/17.7% Al<sub>2</sub>O<sub>3</sub> composite coatings, respectively, illustrating the grain orientation and microstructure within the coatings. The coatings underwent severe plastic deformation due to the high velocity impact. The surfaces were characterized by small grains surrounding large grains. The appearance of this structure is attributed to the localized distortion of particles concentrated at the particle interface during rapid collisions. In other words, a large amount of energy from particle impact was taken up by the particle surface, leading to particle refinement. High-speed particle impacts led to the accumulation of high dislocation densities, which further caused dynamic recrystallization, resulting in grain refinement. Crystal rotation is evident from the color gradient variations in Figure 8a,d, where the assorted color gradients represent different grain orientations. Furthermore, it can be observed that the introduction of Al<sub>2</sub>O<sub>3</sub> particles led to a greater degree of deformation of Al particles in the coating, accompanied by an increase in the number of small-sized grains. Figure 8c,f displays the grain size distribution of the Al coating and Al/17.7% Al<sub>2</sub>O<sub>3</sub> composite coating. The average grain size of the coating decreased from 1.68 μm to 1.47 μm after the addition of Al<sub>2</sub>O<sub>3</sub> particles. Figure 8b,e shows the KAM plots of the Al coating and the Al/17.7% Al<sub>2</sub>O<sub>3</sub> composite coating, respectively, which are used to check the residual compressive stress in the grains. It is evident from the plots that the residual compressive stress generated inside the grains of the Al/17.7% Al<sub>2</sub>O<sub>3</sub> composite coating was higher than that of the Al coating. Moreover, in Figure 2, we see that the XRD peaks shifted towards higher angles, indicating a reduction in interplanar spacing, in accordance with Bragg's law. This confirms the presence of residual compressive stress in the coating which induced crystal rotation and led to the creation of substructures in the coating. The presence of residual compressive stresses also contributed to the enhanced hardness of the composite coating.

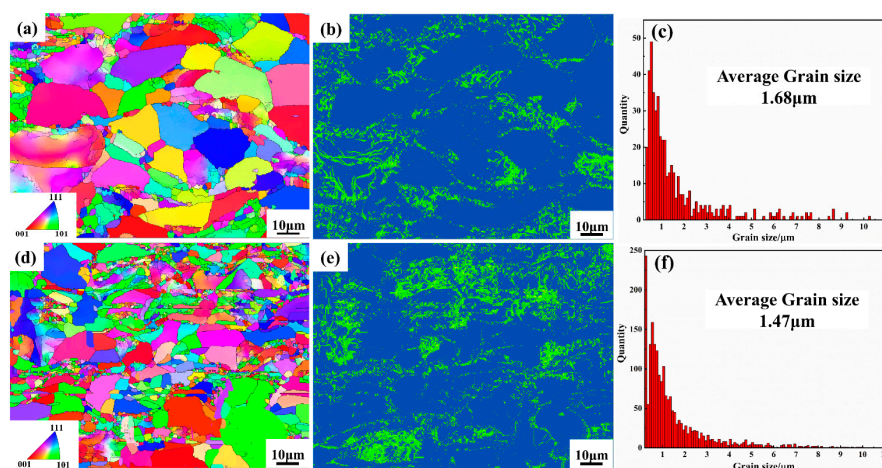


**Figure 8.** EBSD inverse pole figure (IPF) maps, kernel average misorientation (KAM) and grain size distribution for different coatings: (a–c) Al coating, (d–f) Al/17.7% Al<sub>2</sub>O<sub>3</sub> composite coating.

Electrochemical tests showed that the incorporation of Al<sub>2</sub>O<sub>3</sub> particles significantly reduced the degree of corrosion of the composite coating. Several factors contributed to the increase in corrosion resistance. Firstly, the inherent disadvantages of the cold spray

technique resulted in a high porosity in the coating. The entry of electrolyte solution into these pores increases the specific surface area of the corrosion reaction. The addition of hard alumina particles can compact the coating, making the surface denser, reducing porosity. This makes it more difficult for the electrolyte to penetrate the interior of the coating, thereby enhancing the corrosion resistance of the composite coating. Secondly, after adding  $\text{Al}_2\text{O}_3$  particles, the grains of the composite coating are refined, the grain size is reduced, and the grain boundary densities of the composite coatings are increased. The oxidation reactions preferentially occur at the grain boundaries due to their higher energy, and the increased density of these boundaries promotes the formation of  $\text{Al}_2\text{O}_3$  from Al and  $\text{O}_2$ . This results in the formation of a barrier layer of  $\text{Al}_2\text{O}_3$  on the coating surface, which improves its corrosion resistance. Thirdly the addition of  $\text{Al}_2\text{O}_3$  particles improves the corrosion resistance of the composite coating. This is due to the reduction in the exposed area of the Al matrix after the addition. The corrosion resistances of Al/25.5%  $\text{Al}_2\text{O}_3$  and Al/33.3%  $\text{Al}_2\text{O}_3$  composite coatings are weaker than that of the Al/17.7%  $\text{Al}_2\text{O}_3$  composite coating. This is because more  $\text{Al}_2\text{O}_3$  particles will be broken due to collision when the amount of  $\text{Al}_2\text{O}_3$  particles added exceeds 17.7%. The broken  $\text{Al}_2\text{O}_3$  particles will create additional weak bonding surfaces in the coating, and the electrolyte solution can more easily enter the coating's interior through the weak bonding surfaces. Figure 9 shows a schematic diagram of the corrosion principle of the coating before and after the addition of  $\text{Al}_2\text{O}_3$  particles, depicting the grain refinement caused by the addition of  $\text{Al}_2\text{O}_3$  particles as well as the fragmentation of  $\text{Al}_2\text{O}_3$  particles. The addition of  $\text{Al}_2\text{O}_3$  particles led to a large plastic deformation of the Al particles, resulting in the closure of the micropores in the composite coating and the densification of the coating. At the same time, the grains of the composite coating were refined. The corrosion resistance of the composite coating was improved by the combined effect of these changes.

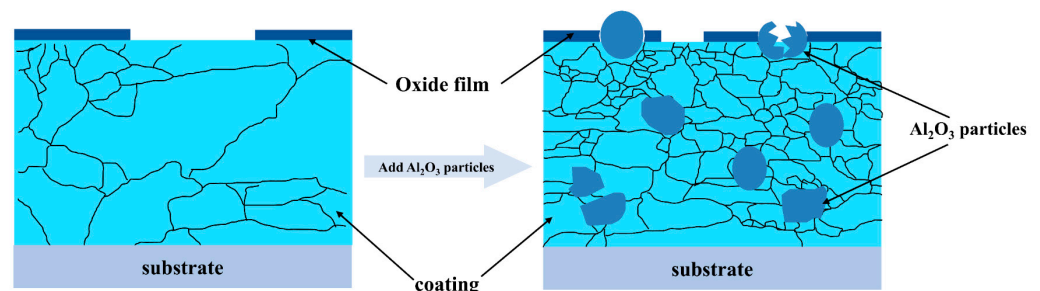


**Figure 9.** Schematic representation of the effect of  $\text{Al}_2\text{O}_3$  particle addition on coating.

## 5. Conclusions

The Al/ $\text{Al}_2\text{O}_3$  composite coatings were deposited on No. 45 steel by cold spraying. The structure and characteristics of the Al/ $\text{Al}_2\text{O}_3$  coatings were systematically investigated. The inclusion of  $\text{Al}_2\text{O}_3$  particles led to a more significant plastic transformation of the previously deposited Al particles, resulting in a denser coating. Compared to the cold-sprayed Al coating, the grains in the Al/ $\text{Al}_2\text{O}_3$  composite coatings were refined, and the residual compressive stress and hardness were increased. The porosity and surface roughness of composite coatings initially decreased and then increased with the amount of  $\text{Al}_2\text{O}_3$  particles. The composite coating with Al/17.7%  $\text{Al}_2\text{O}_3$  had the lowest porosity and showed the best corrosion resistance. The promotion of a corrosion-resistant layer on the surface of the Al/ $\text{Al}_2\text{O}_3$  composite coating was facilitated by the refinement of grains. The corrosion current density of the composite coating was  $2.67 \times 10^{-6} \text{ A/cm}^2$ , which is significantly lower than the corrosion current density of the pure Al coating, at  $1.09 \times 10^{-3} \text{ A/cm}^2$ . If the amount of added  $\text{Al}_2\text{O}_3$  particles exceeds 17.7%, some of the  $\text{Al}_2\text{O}_3$  will break. The broken  $\text{Al}_2\text{O}_3$  particles result in a slight increase in the porosity and roughness of the composite coating, and will create more weak bonding surfaces in the composite coating. These weak bonding surfaces provide channels for the electrolyte to enter the interior of the coating, leading to a decrease in the corrosion resistance of the composite coating.

The addition of Al<sub>2</sub>O<sub>3</sub> particles to the cold spray Al coating will significantly impact the microstructure of the resulting Al/Al<sub>2</sub>O<sub>3</sub> composite coating, affecting both its mechanical properties and corrosion behavior.

**Author Contributions:** W.J. contributed to the conceptualization, methodology, data curation, writing—original draft preparation, funding acquisition, writing—reviewing and editing. X.S. performed visualization, data curation, writing—original draft preparation and formal analysis. Z.W. and Y.L. performed conceptualization, formal analysis, validation. X.Z. and J.Z. contributed to the validation. E.W. helped with the methodology, and the writing—reviewing and editing. All authors have read and agreed to the published version of the manuscript.

**Funding:** This work was supported by Heilongjiang Provincial Natural Science Foundation of China (LH2020E084), the Key Research and Development Program of Heilongjiang (Grant No. 2022ZX01A01), and the National Natural Science Foundation of China (51901058).

**Data Availability Statement:** The original contributions presented in the study are included in the article, further inquiries can be directed to the corresponding author/s.

**Conflicts of Interest:** The authors declare no conflicts of interest.

## References

1. Trueba, M.; Trasatti, S.P. Study of Al alloy corrosion in neutral NaCl by the pitting scan technique. *Mater. Chem. Phys.* **2010**, *121*, 523–533. [\[CrossRef\]](#)
2. Diab, M.; Pang, X.; Jahed, H. The effect of pure aluminum cold spray coating on corrosion and corrosion fatigue of magnesium (3% Al-1% Zn) extrusion. *Surf. Coat. Technol.* **2017**, *309*, 423–435. [\[CrossRef\]](#)
3. Fernandez, R.; Jodoin, B. Cold Spray Aluminum-Alumina Cermet Coatings: Effect of Alumina Content. *J. Therm. Spray Technol.* **2018**, *27*, 603–623. [\[CrossRef\]](#)
4. Bu, H.Y.; Yandouzi, M.; Lu, C.; MacDonald, D.; Jodoin, B. Cold spray blended Al+Mg<sub>17</sub>Al<sub>12</sub> coating for corrosion protection of AZ91D magnesium alloy. *Surf. Coat. Technol.* **2012**, *207*, 155–162. [\[CrossRef\]](#)
5. Liu, H.H.; Tariq, N.U.; Ren, Y.P.; Zhao, L.J.; Yang, Y.; Cui, X.Y.; Wang, J.Q.; Xiong, T.Y. Influence of Al<sub>2</sub>O<sub>3</sub> content on microstructure, electrical conductivity and adhesion strength of cold sprayed Al-Al<sub>2</sub>O<sub>3</sub> coatings on PEEK substrate. *Surf. Coat. Technol.* **2022**, *446*, 128752. [\[CrossRef\]](#)
6. Li, Q.L.; Yuan, S.M.; Li, Z.; Gao, X.X.; Chen, B.C. Mechanical response and microstructure evolution of SiC particle-reinforced Al-MMCs under ultrasonic loading. *Compos. Part A Appl. Sci. Manuf.* **2023**, *173*, 107657. [\[CrossRef\]](#)
7. Zhao, L.J.; Tariq, N.U.; Ren, Y.P.; Liu, H.H.; Han, R.F.; Cui, X.Y.; Wang, J.Q.; Xiong, T.Y. Effect of Particle Size on Ceramic Particle Content in Cold Sprayed Al-Based Metal Matrix Composite Coating. *J. Therm. Spray Technol.* **2022**, *31*, 2505–2516. [\[CrossRef\]](#)
8. Liu, H.J.; Fu, M.K.; Pang, S.Z.; Zhu, H.Q.; Zhang, C.; Ming, L.J.; Liu, X.Y.; Ding, M.H.; Fu, Y.D. Effect of Ball-Milled Feedstock Powder on Microstructure and Mechanical Properties of Cu-Ni-Al-Al<sub>2</sub>O<sub>3</sub> Composite Coatings by Cold Spraying. *Coatings* **2023**, *13*, 948. [\[CrossRef\]](#)
9. Witharamage, C.S.; Alrizqi, M.A.; Chirstudasjustus, J.; Darwish, A.A.; Ansell, T.; Nieto, A.; Gupta, R.K. Corrosion-resistant metallic coatings for aluminum alloys by cold spray. *Corros. Sci.* **2022**, *209*, 110720. [\[CrossRef\]](#)
10. Sayahlatifi, S.; Zaiemyekheh, Z.; Shao, C.W.; McDonald, A.; Hogan, J.D. Micromechanical damage analysis of Al-Al<sub>2</sub>O<sub>3</sub> composites via cold-spray additive manufacturing. *Int. J. Mech. Sci.* **2023**, *259*, 108573. [\[CrossRef\]](#)
11. Chen, H.; Liu, C.; Chu, X.; Zhang, T.; Zheng, J. Corrosion Behavior and Microstructure of Cu-Based Composite Coatings Deposited by Cold Spraying. *Metals* **2022**, *12*, 955. [\[CrossRef\]](#)
12. Aubanel, L.; Delloro, F. Tribological behavior of steel-based composite coatings produced by cold spray. *Surf. Coat. Technol.* **2023**, *470*, 129815. [\[CrossRef\]](#)
13. Bakar, I.A.A.; Omar, N.I.; Yusuf, Y.; Rahim, T.A. Reflection and Future Perspectives in Cold Spray Technology: A Bibliometric Analysis. *J. Therm. Spray Technol.* **2023**, *32*, 1576–1595. [\[CrossRef\]](#)
14. Huang, C.J.; List, A.; Wiehler, L.; Schulze, M.; Gärtner, F.; Klassen, T. Cold spray deposition of graded Al-SiC composites. *Addit. Manuf.* **2022**, *59*, 17. [\[CrossRef\]](#)
15. Ilyushchanka, A.P.; Baray, S.G.; Letsko, A.I.; Talako, T.L.; Manoila, Y.D.; Janu, Y.; Chauhan, V.S.; Patra, M.K.; Saini, L. High-Temperature-Resistant, Mechanically Stable FeCrNiAl/Al<sub>2</sub>O<sub>3</sub> Thermally Sprayed Thick Ceramic Coatings for Stealth Applications over X-Band. *Adv. Eng. Mater.* **2022**, *24*, 103116. [\[CrossRef\]](#)
16. Gül, H.; Kiliç, F.; Aslan, S.; Alp, A.; Akbulut, H. Characteristics of electro-co-deposited Ni-Al<sub>2</sub>O<sub>3</sub> nano-particle reinforced metal matrix composite (MMC) coatings. *Wear* **2009**, *267*, 976–990. [\[CrossRef\]](#)
17. Jue, J.B.; Gu, D.D.; Chang, K.; Dai, D.H. Microstructure evolution and mechanical properties of Al-Al<sub>2</sub>O<sub>3</sub> composites fabricated by selective laser melting. *Powder Technol.* **2017**, *310*, 80–91. [\[CrossRef\]](#)
18. Konstantiniuk, F.; Tkadletz, M.; Czettl, C.; Schalk, N. Fracture Properties of  $\alpha$ - and  $\kappa$ -Al<sub>2</sub>O<sub>3</sub> Hard Coatings Deposited by Chemical Vapor Deposition. *Coatings* **2021**, *11*, 1359. [\[CrossRef\]](#)

19. Wang, Y.Y.; Normand, B.; Mary, N.; Yu, M.; Liao, H.L. Effects of ceramic particle size on microstructure and the corrosion behavior of cold sprayed SiC<sub>p</sub>/Al5056 composite coatings. *Surf. Coat. Technol.* **2017**, *315*, 314–325. [[CrossRef](#)]
20. Yang, X.; Li, W.; Yu, S.; Xu, Y.; Hu, K.; Zhao, Y. Electrochemical characterization and microstructure of cold sprayed AA5083/Al<sub>2</sub>O<sub>3</sub> composite coatings. *J. Mater. Sci. Technol.* **2020**, *59*, 117–128. [[CrossRef](#)]
21. Xie, X.L.; Hosni, B.; Chen, C.Y.; Wu, H.J.; Li, Y.L.; Chen, Z.; Verdy, C.; Kedim, O.E.I.; Zhong, Q.D.; Addad, A.; et al. Corrosion behavior of cold sprayed 7075Al composite coating reinforced with TiB<sub>2</sub> nanoparticles. *Surf. Coat. Technol.* **2020**, *404*, 126460. [[CrossRef](#)]
22. Qiu, X.; Tariq, N.U.; Qi, L.; Tang, J.R.; Cui, X.Y.; Du, H.; Wang, J.Q.; Xiong, T.Y. Effects of Dissimilar Alumina Particulates on Microstructure and Properties of Cold-Sprayed Alumina/A380 Composite Coatings. *Acta Metall. Sin. Engl. Lett.* **2019**, *32*, 1449–1458. [[CrossRef](#)]
23. Wang, Q.; Birbilis, N.; Huang, H.; Zhang, M.X. Microstructure characterization and nanomechanics of cold-sprayed pure Al and Al-Al<sub>2</sub>O<sub>3</sub> composite coatings. *Surf. Coat. Technol.* **2013**, *232*, 216–223. [[CrossRef](#)]
24. Zhang, Z.C.; Liu, F.C.; Han, E.H.; Xu, L. Mechanical and corrosion properties in 3.5% NaCl solution of cold sprayed Al-based coatings. *Surf. Coat. Technol.* **2020**, *385*, 125372. [[CrossRef](#)]
25. Qiu, X.; Tariq, N.U.; Wang, J.Q.; Tang, J.R.; Gyansah, L.; Zhao, Z.P.; Xiong, T.Y. Microstructure, microhardness and tribological behavior of Al<sub>2</sub>O<sub>3</sub> reinforced A380 aluminum alloy composite coatings prepared by cold spray technique. *Surf. Coat. Technol.* **2018**, *350*, 391–400. [[CrossRef](#)]
26. Lu, F.F.; Ma, K.; Li, C.X.; Yasir, M.; Luo, X.T.; Li, C.J. Enhanced corrosion resistance of cold-sprayed and shot-peened aluminum coatings on LA43M magnesium alloy. *Surf. Coat. Technol.* **2020**, *394*, 125865. [[CrossRef](#)]
27. Liu, F.; Han, E.H.; Xu, L.; Uzoma, P.C. Effects of Al<sub>2</sub>O<sub>3</sub> on the microstructures and corrosion behavior of low-pressure cold gas sprayed Al 2024-Al<sub>2</sub>O<sub>3</sub> composite coatings on AA 2024-T3 substrate. *Surf. Coat. Technol.* **2019**, *9*, 735–742.
28. Mansfeld, F.; Jeanjaquet, S.L.; Kendig, M.W. An electrochemical impedance spectroscopy study of reactions at the metal/coating interface. *Corros. Sci.* **1986**, *26*, 735–742. [[CrossRef](#)]
29. da Silva, F.S.; Bedoya, J.; Dosta, S.; Cinca, N.; Cano, I.G.; Guilemany, J.M.; Benedetti, A.V. Corrosion characteristics of cold gas spray coatings of reinforced aluminum deposited onto carbon steel. *Corros. Sci.* **2017**, *114*, 57–71. [[CrossRef](#)]
30. Conde, A.; de Damborenea, J.J. Electrochemical impedance spectroscopy for studying the degradation of enamel coatings. *Corros. Sci.* **2002**, *44*, 1555–1567. [[CrossRef](#)]
31. Chen, H.X.; Kong, D.J. Comparison on electrochemical corrosion performances of arc and laser thermal sprayed Al-Ti-Ni coatings in marine environment. *Mater. Chem. Phys.* **2020**, *251*, 123200.

**Disclaimer/Publisher’s Note:** The statements, opinions and data contained in all publications are solely those of the individual author(s) and contributor(s) and not of MDPI and/or the editor(s). MDPI and/or the editor(s) disclaim responsibility for any injury to people or property resulting from any ideas, methods, instructions or products referred to in the content.